Modelling dust transport in DIII-D with DTOKS-Upgrade

Modelling dust transport in DIII-D with DTOKS-Upgrade

L. Simons,[1, a)] C. Cowley,[1] P. Fuller,[1] I. Bykov,[2] D. Rudakov,[2] Y. Andrew,[1] and M. Coppins[1]
[1)] *Blackett Laboratory, Imperial College, London SW7 2AZ United Kingdom*
[2)] *University of California, San Diego, La Jolla, California 92093-0417, USA*

(Dated: 5 January 2021)

Comprehensive upgrades to the dust transport code DTOKS that extend the plasma-dust interaction model are presented and compared with recent measurements of dust transport in DIII-D. Simulations incorporating variation in physical properties of graphite dust with temperature and size in a stationary plasma background suggest a substantial decrease in lifetimes due principally to thermal expansion. The trajectories of 53 dust grains identified from analysis of visible camera data taken across two similar shots were used to measure the dust particle velocity distributions. Dust tracks terminated mostly at the outer divertor strike point having a mean observation time of $2.1 \pm 0.4ms$. Stochastic modelling of 200 graphite dust particles in the DIII-D tokamak performed with DTOKS-U using plasma simulations generated by OEDGE found similar behaviour, with particles ablating rapidly after acquiring a positive charge in the region close to the outer strike point, creating an acute source of neutral carbon atoms. The simulated mean lifetime, $11 \pm 2ms$, showed approximate agreement with experimental observation when corrected by accounting for dust visibility and ignoring the longest trajectories $1.5 \pm 0.2ms$. Synthetic diagnostic data generated from coupling the results of DTOKS-U with the visualisation software Calcam offers a powerful new tool for validation of simulations and predictive calculations of dust dynamics.

Keywords: Dust, Simulation, Tokamaks

I. INTRODUCTION

The study of the dynamics of small particles in plasmas is relevant to a large number of astrophysical and laboratory environments[1–5] with applications in modelling space shuttle dynamics, plasma diagnostics, planetary systems and dust transport in magnetic confinement fusion devices[6–9]. For tokamaks in particular, knowledge of the motion of dust grains can be critical for correctly modelling core density and radiation balance as well as maintaining long term operational safety and stability[10,11]. Equally important is predicting the motion of cryogenic pellets, which are used increasingly for disruption mitigation and controlling density profiles[12].

Dust is a ubiquitous component of tokamak plasmas that is generated through erosion of the plasma facing components (PFCs) by arcing, localised melting and possibly also bubble burst phenomena[13,14]. The need to avoid the excessive tritium retention by carbon, necessitates the use of beryllium and tungsten PFCs. Measurements in the JET and DIII-D tokamaks have recorded dust inventories of 210g[15] and 90-120g[16] respectively whilst in next generation tokamaks such as ITER, there is predicted to be a high dust production rate[18] of between 78-155kg/yr[17].

The amount of dust accumulated in a few $500s$ long discharges poses a significant threat to the safe operation of ITER in a number of ways[18]. During operation with tritium, fusion plasmas become a radiological hazard as material surfaces can retain an amount of radioactive tritium, causing additional difficulties during decommissioning and shut-down periods of the machine[10]. Dust inventories are further limited by the possibility for environmental contamination in the case of an accidental reactor leak, in which micron sized radioactive particles are released[17]. Moreover, the possibility for toxic beryllium dust of breathable size to escape the reactor chamber is a serious health concern, which also imposes restrictions on dust production in future experiments[10,19].

Atoms that enter the plasma are rapidly ionised and radiate energy through line radiation, recombination and Bremstrahlung radiation, meaning elements with a high atomic number, Z, such as tungsten radiate intensely. In order to achieve break-even conditions[11], the fraction of tungsten ions in the core plasma must remain small, below 3×10^{-5} in the ASDEX tokamak for example[9]. The main source of tungsten impurities and dust in ITER will be the tungsten divertor. In a detached divertor regime, mobilization and penetration of dust into the core plasma and subsequent ablation can contribute a major source of tungsten impurities.

Dust tracking codes have been developed for the purpose of understanding dust dynamics, predicting maximum attainable speeds, potential impact damage to PFCs, dust accumulation sites as well as the associated material migration and lifetimes. An important feature of surface-plasma interactions is the charging and formation of a sheath which shields the charged body from the surrounding plasma[20]. This affects the flux of plasma ions and electrons to the surface, which in turn define the heat and momentum fluxes[21,22]. The majority of dust tracking codes[23–26] calculate these fluxes using the Shifted Orbital Motion Limited (SOML)[20] approach, accounting for a dust velocity relative to the plasma by assuming a shifted Maxwellian background plasma[27]. These theories assume the sphere of radius

[a)] Electronic mail: ls5115@ic.ac.uk

a_d is much smaller than the Debye length, λ_d, which is typically $\lambda_d \simeq 100\mu m$ for a tokamak Scrape Off Layer (SOL) plasma. Additionally, these models assume that the physical properties of dust particles such as expansivity, emissivity and heat capacity assume values that are fixed irrespective of dust temperature or size.

The need to address these problems, and the growing interest in pellet simulation driven by the advent of shattered pellet injection[30,31], has directed much recent research into analytical formula for charging of large emitting dust grains in magnetic fields[23,32,33]. The absence of a formulation for the floating surface potential for all dust sizes and magnetic field strengths has so far limited simulation scope to small dust sizes. This paper details improvements to the DTOKS code focused on modelling the variation of the physical properties of dust with temperature and size and exploring the influence of magnetic fields on dust surface potential. The results are verified against known analytical results and compared to novel observations of dust transport in the DIII-D tokamak.

II. DTOKS-U METHODOLOGY

The original Dust in TOKamaks (DTOKS) code developed at Imperial College, London[35] simulates the forces, currents and mass exchange experienced by an isolated conducting sphere. The code has been implemented in modelling dust in the Mega Amp Spherical Tokamak (MAST)[36], JET[34,37] and ITER[38,39]. The upgraded Dust in TOKamakS code (DTOKS-U) code has overhauled the original, simplifying the operation and implementation of different physics best suited to coping with a broader range of tokamak plasma conditions. In particular, more accurate models accounting for the variability of standard values with dust temperature and size have been introduced along with charging models that provide the currents for dust which are large relative to the plasma Debye length and in plasmas with strong magnetic fields.

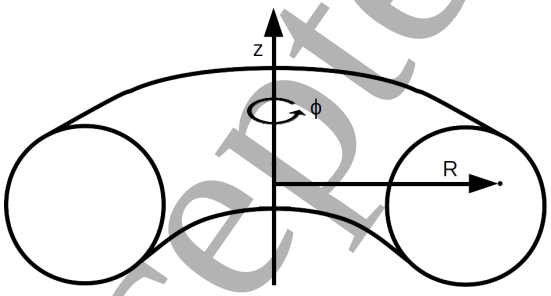

FIG. 1: Schematic of geometry used in DTOKS-U.

DTOKS-U utilises a cylindrical coordinate system, (R, ϕ, z), as shown in figure 1, with an assumed toroidal symmetry of the plasma such that, when performing tokamak simulations, only a two dimensional plasma background in (R, z) is used to model the plasma in three dimensions. Several assumptions common to all dust tracking codes are made in isolating the regime of applicability. The high thermal and electrical conductivity of the materials and relatively small size is assumed to be such that there are no temperature gradients inside the material and negligible surface currents. Purely single elemental composition is taken, with physical properties equal to those of bulk materials, unless otherwise stated. The plasma flow velocity is assumed to be parallel to the magnetic field lines and the number density of dust is considered sufficiently low to ignore dust-dust interactions. The intrinsic and induced magnetic moments due to rotation of these charged conductors are ignored along with their effects on the surrounding plasma.

A. Governing Equations

DTOKS-U solves three non-linear, ordinary differential equations explicitly in time. These equations represent the particle motion, heating and mass loss along with a fourth time independent transcendental equation for the potential. Each process evolves over a unique timescale, with the timescale for charge equilibration in the plasma being approximately given by the electron plasma frequency $\omega_{pe}^{-1} \simeq 2 \times 10^{-11} s$ (for a hydrogen plasma with electron density $n_e = 10^{18} m^{-3}$). This is invariably the fastest timescale for dust grains in tokamaks, meaning charge equilibration almost always occurs more quickly than motion across gradients in plasma conditions, $\lambda_d / |\underline{v}_d| \simeq 10^{-4} m / 100 m s^{-1} = 10^{-6} s$, where $\underline{v}_d$ is the dust velocity or changes in temperature of $\Delta T_d = 1K$ estimated by, $4\pi a_d \rho_d C_v \Delta T_d / 3\Xi \sim 10^{-6} s$, for dust radius $a_d = 1\mu m$, density of carbon $\rho_d = 2260 kg m^{-3}$, heat capacity $C_v = 10^3 J kg^{-1} K^{-1}$[54] and heat flux $\Xi = 10 MW m^{-2}$. This disparity in timescales between charging and other physical processes justifies the assumption of computing the surface potential independently.

1. Charging Equation

The equilibrium charge of spherical dust grains is determined by calculating the surface potential, ϕ_d, under the condition that the sum of the currents to the surface is zero, $\sum_k I_k = 0$. In addition to the currents of plasma ions with effective charge Z and electrons, $I_i = Ze\Gamma_i$ and $I_e = -e\Gamma_e$, due to fluxes of ions, Γ_i, and electrons, Γ_e, it is also necessary to consider the current of secondary and thermionically emitted electrons, I_{see} and I_{tee}. Presently, the currents due to impurity ions are neglected since they are not included in the background plasma used to perform the DTOKS simulations in this work. Accordingly, the drag force and heat flux associated with impurity ions is neglected from the equation of motion and temperature evolution discussed later in sections II A 2 and II A 3. The current balance equation being solved then becomes

$$I_i - I_e + I_{see} + I_{tee} = 0. \quad (1)$$

As mentioned previously, many analytical models exist to describe the currents of ions and electrons in different regimes. For this reason, DTOKS-U is able to operate with several different charging models relevant to different local plasma conditions. These models are extensions of the OML model, with Shifted Orbital Motion Limited (SOML)[27] accounting for flowing plasmas, Shifted Modified Orbital Motion Limited (SMOML)[28] covering large dust in flowing plasmas and Magnetic Field Orbital Motion Limited (MFOML)[40] modelling dust in strong magnetic fields without flow. The SOML and SMOML models are defined by the fluxes $\Gamma_e^{OML}, \Gamma_i^{SOML}, \Gamma_i^{SMOML}$ while Magnetic Field OML (MFOML) refers to the semi-empirical model for the fluxes Γ_i^{MFOML} and Γ_e^{MFOML} as a function of magnetic field strength[40]. The SOML and MFOML models coincide with the OML theory for no flow and in the absence of magnetic fields respectively, whilst SMOML and SOML become equivalent in the limit of infinite flow velocity. By default, the DTOKS-U simulations described in section III use plasma fluxes given by the MFOML model for negatively charged dust and reverts to SOML for positively charged dust.

For the case of small dust grain radius relative to the Debye length, $a_d \leq \lambda_d$, without significant electromagnetic fields, the classical OML theory[7] provides an accurate description of the flux of electrons of mass m_e and with temperature, T_e, to a positive or negatively charged dust grain as

$$\begin{aligned} \Gamma_e^{OML} &= n_e\sqrt{\frac{k_B T_e}{2\pi m_e}}e^{\chi}, && \chi \geq 0 \\ \Gamma_e^{OML} &= n_e\sqrt{\frac{k_B T_e}{2\pi m_e}}(1+\chi), && \chi < 0. \end{aligned} \tag{2}$$

The plasma is assumed to be quasi-neutral with ions and electrons having densities far from the dust surface n_i and n_e that are approximately equal. The normalised surface potential, χ, is defined by $\chi = -e\phi_d/k_B T_e$.

For ions of mass m_i flowing at a velocity, U_i, with normalised flow velocity $u_i = U_i/\sqrt{k_B T_i/m_i}$, the SOML theory is used[27], accounting for a shifted Maxwellian background plasma,

$$\begin{aligned} \Gamma_i^{SOML} =& \frac{n_i}{4u_i}\sqrt{\frac{k_B T_i}{m_i}}\Big[\frac{(1+2u_i^2)erf(u_i)}{2} \\ &+ \frac{u_i}{\sqrt{\pi}}e^{-u_i^2} + erf(u_i)\frac{\chi}{\tau}\Big], \qquad \chi \geq 0 \\ \Gamma_i^{SOML} =& n_i\sqrt{\frac{k_B T_i}{m_i}}\Big[\Big(1+2\Big(u_i^2+\frac{\chi}{\tau}\Big)\Big) \\ &(erf(u_p)+erf(u_m))+ \\ &\frac{2}{\sqrt{\pi}}\Big(u_p e^{-u_m^2} + u_m e^{-u_p^2}\Big)\Big], \qquad \chi < 0. \end{aligned} \tag{3}$$

Here, $\tau = T_i/T_e$ is the temperature ratio of ions, T_i, to electrons and the definitions $u_p = u_i + \sqrt{-Z\chi/\tau}$ and $u_m = u_i - \sqrt{-Z\chi/\tau}$ are used.

For larger dust, the OML theory no longer applies and sheath effects must be accounted for. With the SMOML model for negatively charged dust[28], this gives

$$\begin{aligned} \Gamma_i^{SMOML} =& \frac{n_i}{4u}\sqrt{\frac{k_B T_i}{m_i}}\Big[\frac{(1+2u_i^2)erf(u_i)}{2} \\ &- \frac{\chi erf(u_i)}{\tau}\Big[\chi - \frac{1}{2}ln\Big(\frac{2\pi}{\mu^2}(1+\gamma\tau)\Big)\Big] \\ &+ \frac{u_i e^{-u_i^2}}{\sqrt{\pi}}\Big], \qquad \chi \geq 0 \\ \Gamma_i^{SMOML} =& \Gamma_i^{SOML}, \qquad \chi < 0. \end{aligned} \tag{4}$$

Here, $\mu = m_i/m_e$, is the ratio of the ion to electron mass and γ is the ratio of specific heats.

Finally, the presence of a magnetic field of strength, B, alters the charged particle fluxes substantially when the dust size is comparable to or larger than the electron gyro-radius[40]. The MFOML model calculates the potential as a function of the ion magnetisation parameter $\beta_i = eBa_d/m_i v_{T,i} \simeq 10^4 Ba_d/\sqrt{T_i}$ for small dust radii relative to Debye length $\lambda_d/a_d \geq 0.5$ based on a semi-empirical fit to Monte Carlo simulation results of the `pot`[41] and DiMPl[40] codes

$$\begin{aligned} \Gamma_i^{MFOML} &= \frac{n_i}{2}\sqrt{\frac{k_B T_i}{m_i}}\Big[\Big(1+\frac{2Z\chi}{\tau}\Big)e^{-1.56\beta_i^{0.56}} + 1\Big], \\ \Gamma_e^{MFOML} &= \frac{n_e e^{-\chi}}{2}\sqrt{\frac{k_B T_e}{m_e}}\Big[e^{-0.23\beta_e} + 1\Big]. \end{aligned} \tag{5}$$

The electron magnetisation parameter, β_e, is related to the ion magnetisation parameter through the mass and temperature ratios, $\beta_e = \sqrt{\mu\tau}\beta_i$ for a hydrogen plasma. This model deviates from the OML model for $0.5 \leq \beta_i$ and breaks down for positively charged dust. A typical value for the ion magnetisation parameter for a dust radius $a_d = 50\mu m$ in the Scrape Off Layer (SOL) plasma of the DIII-D tokamak with $T_i = 5eV$ and $B = 2T$ is $\beta_i \simeq 0.4$. At this stage, the implementation of the MFOML fluxes in the charge equation 1 is not reflected in the associated ion drag force and heat fluxes of ions and electrons, which are computed using the SOML model. The implementation of MFOML for the forces and heat fluxes is reserved for future works.

At high dust temperatures, T_d, electron emission becomes a dominant term in balancing the charged particle fluxes at the surface as electrons are able to escape the confining atomic potentials. The positive current due to secondary electron emission is defined through δ_{sec} as a fraction of the total electron current $I_{see} = \delta_{sec} I_e$ in the same manner as used previously in DTOKS[45]. The flux of electrons due to thermionic electron emission (TEE), Γ_{th}, is calculated using the Richardson-Dushman Formula[60] as before[45] but with an additional Schottky

correction factor[43] for negatively charged dust

$$\Gamma_{th} = \frac{R_i T_d^2}{e} e^{-\frac{W_f}{k_B T}}, \qquad \chi \geq 0,$$
$$\Gamma_{th} = \frac{R_i T_d^2}{e}\Big(1 - \frac{T_e \chi}{T_d}\Big) e^{-\frac{k_B T_e \chi + e W_f}{k_B T_d}}, \chi < 0. \tag{6}$$

Here, W_f is the work function of the material and $R_i = 1.20173 \times 10^6 A m^{-2} K^{-2}$ is the Richardson constant. For simplicity, the effect of this emitted charged flux on the form of the potential above the surface is neglected in these models. The root of equation 1 is found for an electron and ion current calculated using either the OML, SOML, SMOML or MFOML models in addition to the currents due to electron emission, I_{see} and I_{tee}, via a 1st order Householder method known as the Newton-Raphson method to an arbitrary accuracy A_c.

2. Equation of Motion

The equation of motion for a dust grain of mass, M_d and charge, Q_d, describes the evolution of the dust velocity, $\underline{v}_d$, with time t,

$$M_d \frac{d\underline{v}_d}{dt} = Q_d(\underline{E} + \underline{v}_d \times \underline{B}) + M_d \underline{g} + \underline{F}_{id} + \underline{F}_n. \tag{7}$$

The first three terms due to gravity and the influence of the background electric $\underline{E}$ and magnetic $\underline{B}$ fields are calculated directly from the local plasma parameters where $\underline{g} = (0, 0, -9.81)$ is the acceleration due to gravity. These terms are typically largest for sub-micrometre sized dust but are small relative to the ion drag force, $\underline{F}_{id}$. The rocket force caused by asymmetric ablation over the dust surface is neglected as it is inconsistent with the assumptions of a spherically symmetry, homogeneous and conducting dust grain. The force due to collection and deflection of ions, $\underline{F}_{id}$, is calculated using the hybrid model[46],

$$\underline{F}_{id} = \sqrt{2\pi} a_d^2 n_i m_i v_{T,i}^2 (G_1 + G_2) \frac{(\underline{U}_i - \underline{v}_d)}{|\underline{U}_i - \underline{v}_d|}, \tag{8}$$

where

$$G_1 = \sqrt{\frac{\pi}{2}} erf\Big(\frac{u_i}{\sqrt{2}}\Big)\Big[1 + u_i^2 + \Big(1 - \frac{1}{u_i^2}\Big)(1 + \frac{2\chi}{\tau}) + \frac{4\chi^2 ln(\Lambda_c)}{\tau^2 u_i^2}\Big], \tag{9}$$
$$G_2 = \frac{1}{u_i} e^{-\frac{u_i^2}{2}}\Big(1 + \frac{2\chi}{\tau} + u_i^2 - \frac{4\chi^2 ln(\Lambda_c)}{\tau^2}\Big).$$

This is equivalent to the force calculated using the assumptions of the SOML charging model. Here, the Coulomb logarithm is approximated by

$$ln(\Lambda_c) = log\Big(1 + \frac{\lambda_d \tau (1 + u_i^2)}{a_d \chi_a}\Big). \tag{10}$$

For positively charged dust, this formulation of the Coulomb logarithm is badly specified and the approximation $ln(\Lambda_C) \simeq 17$ is used which is appropriate for weak potentials. The force due to collisions with neutralised ions, $\underline{F}_n$, is given by Epstein drag[44]

$$\underline{F}_n = -\pi a_d^2 m_i n_n \sqrt{\frac{2k_B T_n}{m_i}} \frac{(\underline{U}_n - \underline{v}_d)}{u_n}\Big[\frac{e^{-u_n^2}}{\sqrt{\pi}}\Big(u_n + \frac{1}{2u_n}\Big) + \Big(1 + u_n^2 - \frac{1}{4u_n^2}\Big) erf(u_n)\Big], \tag{11}$$

where the normalised flow velocity is defined as $u_n = |\underline{U}_n - \underline{v}_d| / \sqrt{2k_B T_n / m_n}$ for neutrals flowing with a velocity $\underline{U}_n$ and with a neutral temperature, T_n and density n_n. However, it is assumed that the neutral background particles have zero net flow velocity, $\underline{U}_n = 0$, such that the force always acts in opposition to the dust velocity.

The equation of motion is solved explicitly using a 4th order Runge-Kutta method with a timescale determined by three conditions. Firstly, the acceleration must be $< 0.01 ms^{-2}$ to ensure changes in velocity are resolved to a minimum fixed precision. Secondly, the time-step must be small enough to ensure that the particle does not cross multiple grid cells of width Δl in a single time step. Finally, the gyro-motion of the dust particle travelling at a velocity $v_{d,\perp}$ perpendicular to $\widehat{\underline{B}}$ must be resolved. These conditions are summarised by the following timescales;

$$\Delta t_{m,1} = \frac{0.01}{\Big|\frac{d\underline{v}_d}{dt}\Big|}, \; \Delta t_{m,2} = \frac{\Delta l}{2|\underline{v}_d|}, \; \Delta t_{m,3} = \frac{v_{d,\perp} M_d}{e|\underline{B}|}. \tag{12}$$

The timescale for the equation of motion, Δt_m, is determined from the minimum of these three timescales

$$\Delta t_m = A_m min(\Delta t_{m,1}, \Delta t_{m,2}, \Delta t_{m,3}), \tag{13}$$

up to a user defined accuracy A_m, ensuring the equation is solved to the required precision.

3. Equation of Heating and Mass Loss

The differential equation for the change in dust temperature, T_d, is calculated from the equation defining specific heat, C_v, for the net power flux to the surface P_t

$$P_t = M_d C_v \frac{dT_d}{dt}. \tag{14}$$

Several different terms, P_k, contribute to the total power flux,

$$P_t = 4\pi a_d^2 (P_{rad} + P_{evap} + P_n + P_e + P_i + P_{rec} + P_{tee} + P_{see}), \tag{15}$$

where the symbols, P_k, represent the heat flux intensity due to different sources. The influence of chemical

sputtering on the energy and mass balance is ignored, as sputtering yields are typically small[56]. The power exchange through electromagnetic radiation, P_{rad}, is given by the Stefan-Boltzmann Law,

$$P_{rad} = \epsilon(a_d, T_d)\sigma(T_d^4 - T_a^4), \tag{16}$$

where σ is the Stefan-Boltzmann constant, $\epsilon(a_d, T_d)$ is the emissivity and T_a is the ambient temperature taking a default value of $T_a = 300K$. The heat flux due to neutral bombardment, P_n, is calculated as

$$P_n = n_n\sqrt{\frac{k_B T_n}{m_i}}(T_n - T_d)k_B. \tag{17}$$

The plasma heating terms due to electrons, P_e, and ions, P_i, neutral recombination, P_{rec}, and the heat loss from thermionic and secondary electron emission P_{tee} and P_{see} remain unchanged from their previous implementations[45,59]. Finally, a heat loss due to evaporative cooling, P_{evap}, has been introduced together with the mass lost through this process.

Mass loss is accounted for through heat energy directly breaking bonds at the boiling temperature, T_b, and evaporation through the liquid phase $T_m < T_d < T_b$ where T_m is the melting temperature. The mass loss due to boiling and evaporation respectively are described by

$$\begin{aligned}\frac{dM_d}{dt}|_{T_d=T_b} &= \frac{P_t}{L_v},\\ \frac{dM_d}{dt}|_{T_d\geq T_m} &= A_m\Gamma_{evap}.\end{aligned} \tag{18}$$

With L_v being the latent heat of vaporisation and A_m the atomic mass of the element in kilogrammes. The generic equation used to model the evaporation flux, Γ_{evap}, is the Hertz-Knudsen equation[58]

$$\Gamma_{evap} = \frac{p_v - p_{amb}}{\sqrt{2\pi m_d k_B T_d}}. \tag{19}$$

The corresponding heat flux is calculated from the thermal energy taken by the escaping particle and the binding energy E_b as $P_{evap} = \Gamma_{evap}(3k_BT_d/2 + E_b)$. Here, p_{amb}, is the ambient background pressure which is taken to be $p_{amb} = 0$ as the background density of atoms originating from the dust is small. The vapour pressure, p_v, is a strong function of temperature and is described by an empirical relation known as the Antoine equation[57] having the form,

$$p_v = 10^{A - \frac{B}{T_d}}, \tag{20}$$

with material specific constants A and B[42]. Figure 2 shows the vapour pressure of tungsten, iron and beryllium over their liquid temperature ranges.

The timescale for solving the heating equation, Δt_h, is determined by the condition that the temperature change

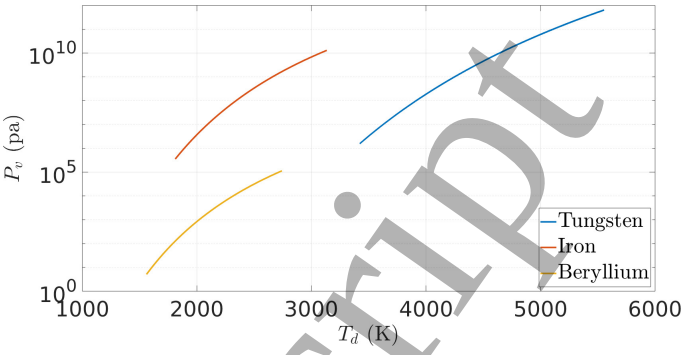

FIG. 2: Vapour pressure as a function of temperature as described by equation 20 for tungsten, iron and beryllium[42].

is less than a specified accuracy, A_h, such that

$$\Delta t_h = \frac{C_v M_d A_h}{P_t}. \tag{21}$$

Since the mass change is evaluated in the same step, it is also required that the mass change is not greater than 1% of the mass preceding that step.

When solving equations 1, 7 and 14 simultaneously, it is often assumed by other dust transport codes that the heating and dynamical timescales are roughly equivalent, meaning they can be solved in an interchangeable order. However, this is not always true and is demonstrable by considering the hotter, dense regions of SOL plasma without significant relative flow velocity. In this case, the heating timescale would be expected to be shorter than the force time scale by up to two orders of magnitude. To avoid unnecessary computational expense in solving the system of equations, it is preferable to take many small steps in the faster varying quantity. This is performed by DTOKS-U when the heating and forcing timescales differ by more than a factor of two.

B. Boundary Conditions

DTOKS-U can be run either with a constant, spatially uniform and infinite plasma background or with a regular rectangular grid provided by a plasma simulation code, with grid spacing Δl_r and Δl_z.

For the spatially uniform plasma, the constant plasma parameters are read directly from the configuration file and simulations only terminate when either the matter sample reaches thermal equilibrium with the plasma or the mass falls below a fixed threshold value. Thermal equilibrium is defined by satisfying one of three conditions: The net power, P_t, to the surface is zero, the rate of change of temperature with time is $< 0.01Ks^{-1}$ or there is a change in the sign of the gradient of the temperature evolution.

When utilising a plasma grid, the plasma parameters for each grid cell are read from a file and stored. The

Elem	a_d (μm)	$T_{i,e}$ (eV)	n_0 (m^{-3})	$\lvert\underline{B}\rvert$ (T)	U (ms^{-1})
C	1	50	10^{18}	2.0	500

TABLE I: Default parameters used by DTOKS-U simulations in section II C.

nearest integer cell coordinates (i,k) to the dust are tracked. The local plasma conditions are determined by a weighted 4^{th} order interpolation method from the nearest grid cell centres and used to define the local plasma conditions. Optionally, two additional files specify the solid boundary of the tokamak PFCs and the core plasma boundary, causing specular reflection at the wall and termination at the core.

The value of the electric field $\underline{E}(i,k) = \underline{E}_r(i,k) + \underline{E}_z(i,k)$ is calculated from the difference in potential $V(i,k)$ between neighbouring grid cells, such that the radial, $\underline{E}_r(i,k)$, and vertical, $\underline{E}_z(i,k)$, electric field components are defined as,

$$\begin{aligned}\underline{E}_r(i,k) &= \frac{V(i+1,k) - V(i-1,k)}{2\Delta l_r}\hat{\underline{r}},\\ \underline{E}_z(i,k) &= \frac{V(i,k+1) - V(i,k-1)}{2\Delta l_z}\hat{\underline{z}}.\end{aligned} \tag{22}$$

With a plasma grid, an additional termination condition is specified which halts simulations if the grain exits the simulation domain.

C. Temperature and size dependence of standard values

Many values typically assumed to be equal to their standard bulk values in dust simulations in fact vary significantly over the relevant range of dust temperatures and sizes. Variations in the emissivity, thermal expansivity and heat capacity are crucial for determining heat fluxes and equilibrium temperatures which in turn determine the ablation rate. The dependency of the heat capacity and thermal expansion on temperature, and of the emissivity on the size and temperature of the material are considered for four fusion relevant elements; beryllium, carbon, iron and tungsten.

At high temperatures, one of the most dominant heat loss terms is black-body radiation from the surface, given by equation 16. A constant emissivity is a poor approximation when considering objects of varying temperatures and sizes comparable to the peak wavelength of emitted radiation[47,48]. To calculate the emissivity, a code developed by Wiscombe[49] was employed to generate a look-up table over the phase space of temperature and dust grain radii. The emissivity was calculated in steps of $1K$ for temperatures from $280K \leq T_d \leq T_B$ for each material and with a pseudo-logarithmic step in radius between $0.01\mu m \leq a_d \leq 100\mu m$. Figure 3 shows $\epsilon(a_d, T_d)$ for the four relevant elements, which varies by more than two orders of magnitude over the parameter

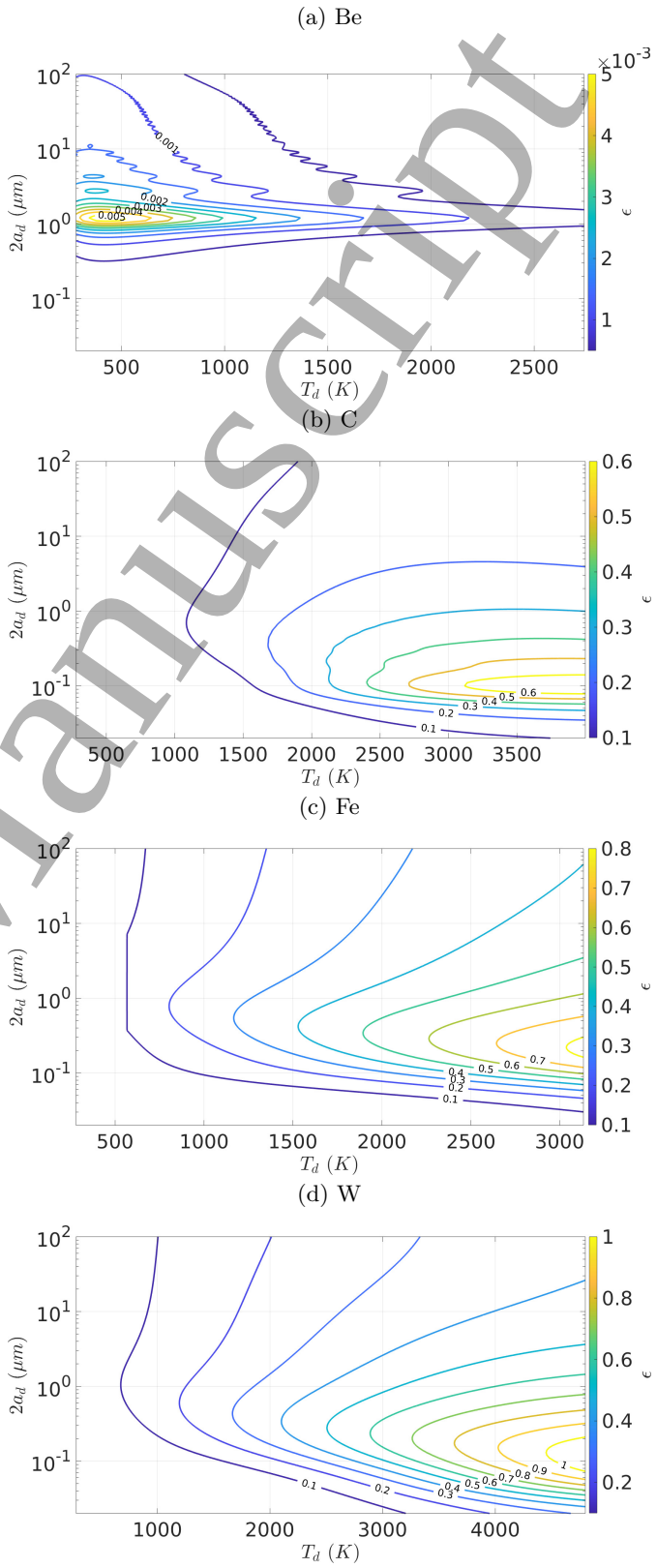

FIG. 3: Dependence of the emissivity of beryllium (3a), carbon (3b), iron (3c) and tungsten (3d) on dust size and temperature calculated using the Wiscombe code[49]
.

space. In general, the emissivity of small metal spheres ($10nm \leq a_d \leq 1\mu m$) is overestimated at low and modest temperatures ($300K \leq T_d \leq 2000K$) compared with using the values relevant for bulk solid samples[48]. This more accurate estimation of the emissivity therefore leads to a slightly higher prediction of the equilibrium temperature as compared with a constant value.

The thermal expansion of materials can affect the dynamics and heating of dust by increasing the flux of particles. This is modeled in DTOKS-U through a semi-empirical formula

$$\frac{a_d(T_d)}{r_0} = 1 + A_1 T_d + A_2 T_d^2 + A_3 T_d^3 + A_4 T_d^4, \qquad (23)$$

where A_{1-4} are material specific constants[50–53] and r_0 is the un-expanded radius. Figure 4 shows the variation of the linear expansion coefficient with dust temperatures from solving equation 23 with different constants A_{1-4} for each element and phase, causing discontinuities at phase boundaries. The maximum change in size is typically around $\sim 30\%$ but for carbon, the thermal expansion is severe causing size changes of up to $\sim 400\%$. The larger radii of thermally expanded dust enhances the influence of collection forces such as ion and neutral drag since there is a larger area for collection by the same mass. This also has an impact on heating timescales by increasing the magnitude of the heat flux and causing a faster approach to equilibrium.

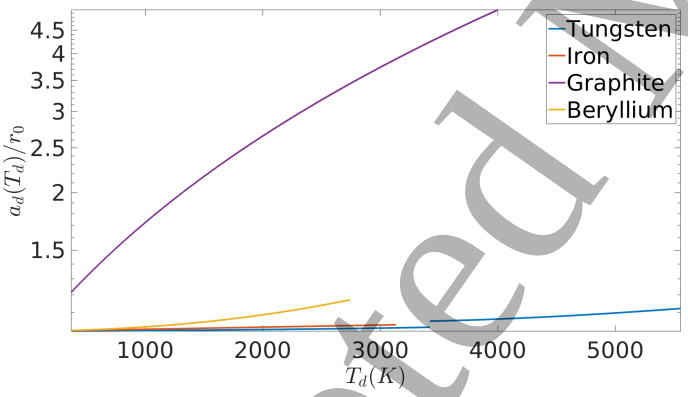

FIG. 4: Dependence of the linear expansion coefficient on temperature for beryllium[50], iron[51], carbon[52] and tungsten[53] spheres modelled by equation 23.

The heat capacity of fusion relevant materials as a function of temperature varies by up to a factor of $\sim 3-5$. This is significant since any change directly affects the total rate of heating of the sample. Similarly to thermal expansion, the heat capacity is approximated by a semi-empirical function of the dust temperature,

$$C_v(T_d) = B_0 + B_1 T_d + B_2 T_d^{-1} + B_3 T_d^{-2} + B_4 T_d^{-3} + B_5 T_d^{-4}. \qquad (24)$$

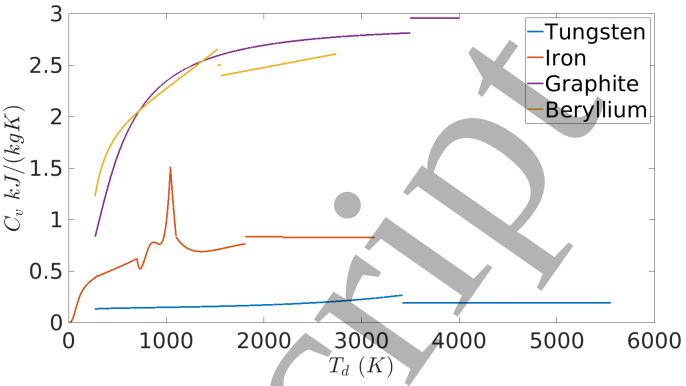

FIG. 5: Dependency of heat capacity on temperature for tungsten[53], iron[51], graphite[54] and beryllium[55] modelled by equation 24. Discontinuities arise during phase changes.

Using unique empirical constants B_{0-5} for tungsten[53], iron[51], graphite[54] and beryllium[55], figure 5 shows the temperature dependant heat capacity given by equation 24. Once more, phase changes produce discontinuities in material properties as modelled by solving equation 24 with different constants B_{0-5}. Changes in the heat capacity have a very obvious and direct impact on the temperature evolution of dust.

The variation in the material properties with temperature introduce feedback effects when conflated with the dependency of the other properties of the dust on size and temperature. To demonstrate this, the simplified case of a carbon dust grain in a constant plasma background was considered by performing simulations with a spatially uniform plasma. The default parameters used in simulations are shown in Table I.

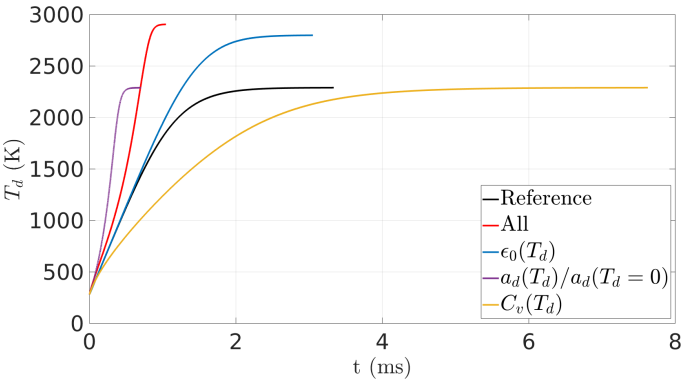

FIG. 6: Simulated temperature evolution of a carbon dust grain in a spatially uniform plasma with properties given by Table I for a reference case with constant standard values and cases with $\epsilon(a_d, T_d)$, $C_v(T_d)$ and $a_d(T_d)/r_0$.

Figure 6 shows the temperature evolution when modelling the variability of $\epsilon(a_d, T_d)$, $C_v(T_d)$ and $a_d(T_d)/r_0$ independently and in combination as compared to a ref-

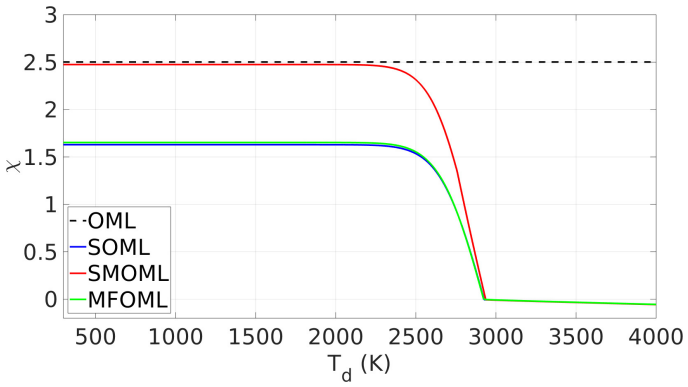

FIG. 7: Dependence of the normalised floating potential, χ, on dust temperature for four different charging models, OML, SOML, SMOML and MFOML.

erence simulation in which all three are fixed ($\epsilon = 0.7$, $C_v = 0.846kJkg^{-1}K^{-1}$ and $a_d = r_0$) at their nominal bulk values. The greater heat capacity of graphite at higher temperatures causes a more gradual approach to equilibrium. Conversely, the thermal expansion of graphite at high temperatures increases the surface area and surface heat fluxes proportionally, causing a more rapid approach to equilibrium. The nominal value of $\epsilon = 0.7$ for graphite is on average larger than the more accurate estimation over the range of sizes and temperatures modelled, leading to a smaller thermal radiation term and larger equilibrium temperatures. The combined effect increases the equilibrium temperature by $\sim 200K$ and halves the time taken to reach equilibrium.

III. SIMULATION VERIFICATION

Where possible, tests validating the behaviour of DTOKS-U for problems with analytical solutions have been conducted. For a charged sphere moving in a vacuum with a constant and uniform force field, there exist analytical solutions for the motion which can be compared to the numerical solution of equation 7 in DTOKS-U. As expected for motion in an electric and gravitational field, the numerical solution matches the analytical solution to machine precision irrespective of time-step size tested. When a magnetic field is introduced, the non linearity of the $\underline{v} \times \underline{B}$ term of the Lorentz force causes the numerical solution to deviate. This cyclotron motion was found to require $A_m = 0.1$ to measure the velocity to a precision of 1%.

When solving equation 14, for a constant value of $P_t = 10^{-11}kW$, the time taken to reach thermal equilibrium and the equilibrium temperatures were found to agree with analytical treatments to an accuracy of less than 0.01% for $A_h = 0.5$.

The addition of new charging models in DTOKS have improved the modelling of charging for large, high temperature dust grains in strong magnetic fields. In figure 7, the charging models SOML (equation 3), SMOML (equation 4), MFOML (equation 5) and the nominal OML charging model are compared. All of these incorporate an electron flux following equation 2 and electron emission processes as described in Section II A 1. At positive potentials, the MFOML model defaults back to the SOML fluxes with electron emission. Figure 7 shows the dependency of the normalised floating potential on the dust temperature of carbon for the four different models. The potential at low dust temperatures is smaller for SOML and MFOML than the OML potential due to secondary electron emission process but comparable for SMOML due to the increase in potential due to inclusion of a plasma sheath. At approximately $T_d \simeq 2900K$, TEE begins to dominate and there is a change in behaviour seen for the SOML, SMOML and MFOML model when $I_{see} + I_{tee} > I_e$. For higher temperatures, the dust becomes gradually more positive as TEE grows stronger and the behaviour is similar for all three models. For this ion magnetisation value $\beta_i = 0.002$, the magnetic field has an insubstantial effect on the equilibrium surface potential so that the MFOML model predicts similar values of surface potential to the SOML model.

IV. 3D TRAJECTORY ANALYSIS IN DIII-D

Validation of the DTOKS-U code has been performed through modelling novel observations of the motion of particles in the divertor of the DIII-D tokamak made by fast visual imaging diagnostic cameras with a pixel resolution of 368×512. The first 2000ms of the two plasma discharges labelled S167342 and S16734 were analysed. The plasma conditions during this time were comparable between the two shots with 1.5MA flat top current, rising NBI heating from 2.5MW to 6.5MW, a toroidal magnetic field of $B_\theta = 2.0T$ and with integrated density $n_e = 2.5 - 7.5 \times 10^{19}m^{-3}$. The field of view of the imaging system is shown in figure 8a while figure 8b shows a superposition of 7 frames with the trajectories of three example particles highlighted. Due to their high temperatures, particles emit thermal radiation and are identified as bright spots or streaks. The black spots are dead channels which were ignored for the purpose of reconstruction.

The locations of particles in each frame and their motion through concurrent frames was reconstructed using the Robust Impurity Detection And Tracking code, RIDAT[62]. A raw total of 932 tracks were identified; 66 in S167342 and 866 from S167345. The plasma termination event occuring at $2000ms$ in S167345 meant that only 37 of the particle tracks in this discharge travelled under nominal plasma conditions. Omitting duplicate tracks and particles with observation times shorter than $1ms$, equivalent to five frames, figure 8c shows a polar plot of the positions of the remaining 53 dust particles, 33 from S167342 and 20 from S167345, in camera coordinates as calibrated from the pixel width of the probe aperture ($120px$) of known width $0.073m$.

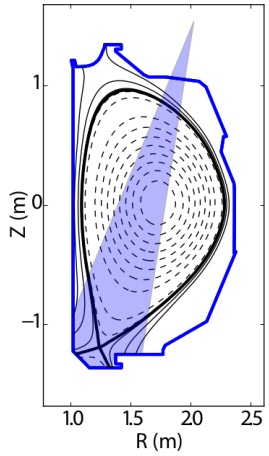

(a) Poloidal cross-section of DIII-D showing the field of view of the visual camera in blue and example magnetic field topology.

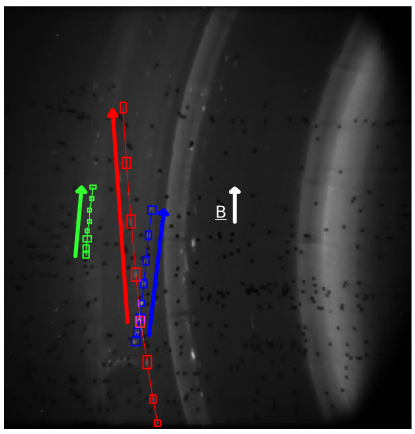

(b) Seven superimposed raw images from S167342 with three trajectories tracked over 49 concurrent frames highlighted in red, blue and green.

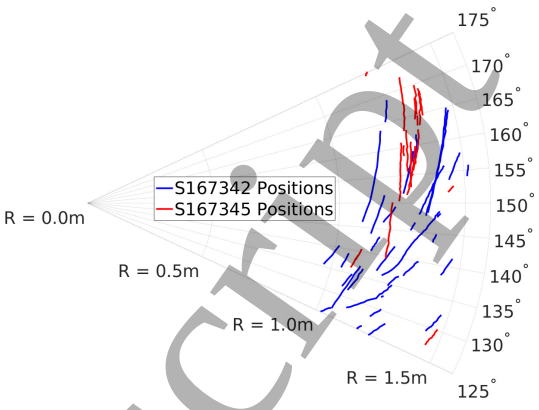

(c) Dust grain positions for S167342 (blue) and S167345 (red) as a function of major radius and absolute toroidal angle, reconstructed using RIDAT.

FIG. 8: Field of view (8a), example image data (8b) and reconstructed tracks (8c) of fast visual imaging camera.

The speeds of dust particles displayed in figure 9 were calculated from the change in position of particles between each frame and the frame rate of the camera (5,000Hz). With the absence of additional information from an orthogonal view, only the motion of particles perpendicular to the camera field of view is measured, with particles assumed to be moving along the divertor floor. The radial speed was fit with a normal distribution whilst the toroidal speeds are fit with a log-normal distribution as shown in figure 9. In general, particles were observed to follow slightly curved trajectories with a significant speed in the toroidal direction in the same sense as the toroidal ion flow. These speeds were found to be in good agreement with previous measurements of dust grain speeds in DIII-D[29].

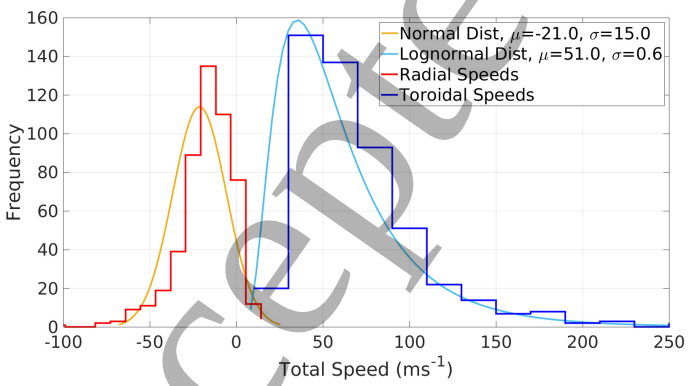

FIG. 9: Dust grain toroidal and radial speeds in DIII-D for both shots S167342 and S167345.

The mean observation time measured was $\tau_{exp} = 2.1ms \pm 0.4ms$ which provides a lower bound for the particle lifetime, since this timescale is also affected by particle brightness and occlusion from the camera view. The acceleration of dust particles in the toroidal and radial direction was calculated from the change in velocity between the first and last frame in which the dust particle was observed. The mean acceleration of particles in the toroidal direction calculated by this method was $a_\theta = 15 \pm 3kms^{-2}$ and $a_R = -4.1 \pm 2.6kms^{-2}$ in the radial direction. However most particles experienced insignificant acceleration during observation, with the majority traversing across the field of view with a constant velocity and many experienced comparable accelerations in the opposite direction. Many particle trajectories were observed to terminate in the bright curved band in the centre of figure 8b corresponding to the location of the outer strike point.

V. SIMULATED TRAJECTORIES

Predictive modelling of the lifetimes of micrometre size carbon spheres has been performed, implementing the methods detailed in section II with initial conditions inferred from the experimental measurements. The speed distributions of figure 9 were used to randomly generate the initial radial and angular velocities of 200 graphite particles using DTOKS-U. The initial temperature of 300K was chosen, with initial positions at a fixed height just above the divertor floor ($z = -1.24m$) and a randomly generated initial radial position uniformly distributed between $1.1m \leq R \leq 1.4m$. The size of particles were selected randomly through inverse transform sampling of the size distribution previously recorded[29], where the fraction of particles of a particular size were found to be $\propto a_d^{-1.4}$. A maximum particle size of $100\mu m$ was set to ensure simulated particles were small relative to the

(a) Simulated plasma density.

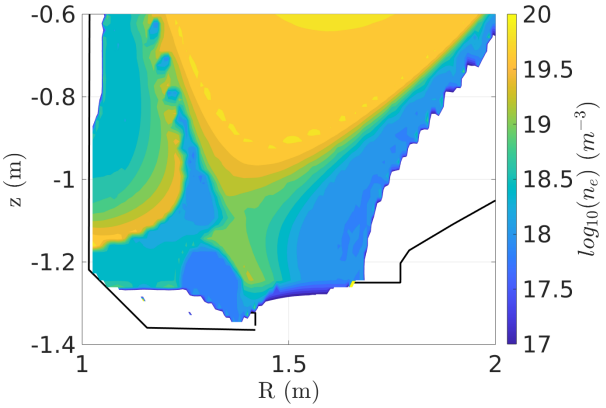

(b) Simulated electron temperature.

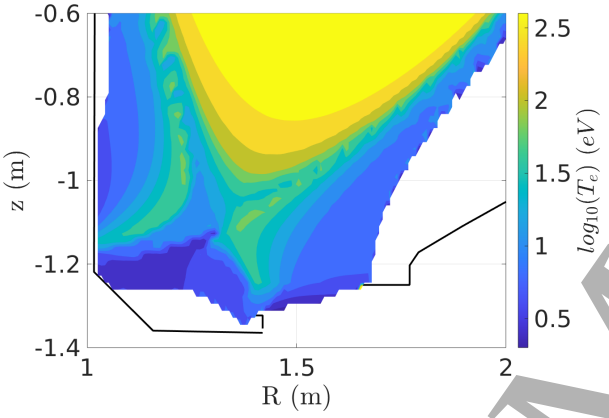

FIG. 10: Poloidal cross-section of DIII-D showing contours of the log of the simulated plasma density (10a) and temperature (10b) (coloured) generated by OEDGE[63] as well as the inner wall boundary (black).

Debye length. The floating potential was determined by solving equation 1 with the MFOML charging model using fluxes given by equation 5 with electron emission.

The plasma parameters were taken from OEDGE simulations[63] of a similar representative shot (S167353) and interpolated onto a regular square grid. Figure 10 shows the simulated plasma density and temperature across a poloidal cross section and the boundary of the inner wall in black. The values are peaked on axis with a single lower null configuration leading to an inner strike point on the inner wall and the outer strike point at the divertor lip edge $(R, z) = (1.4m, -1.25m)$. The plasma conditions in the unspecified regions between the wall and the edge of the plasma were extrapolated from the closest known values at the plasma edge. This has a limited impact on the results as dust remains mostly in the lower divertor close to the x-point.

Figure 11 shows a plan view of the dust trajectories simulated in DTOKS-U superimposed on the simulated electron temperature at $z = -1.25m$. Since the initial

(a) Short trajectories.

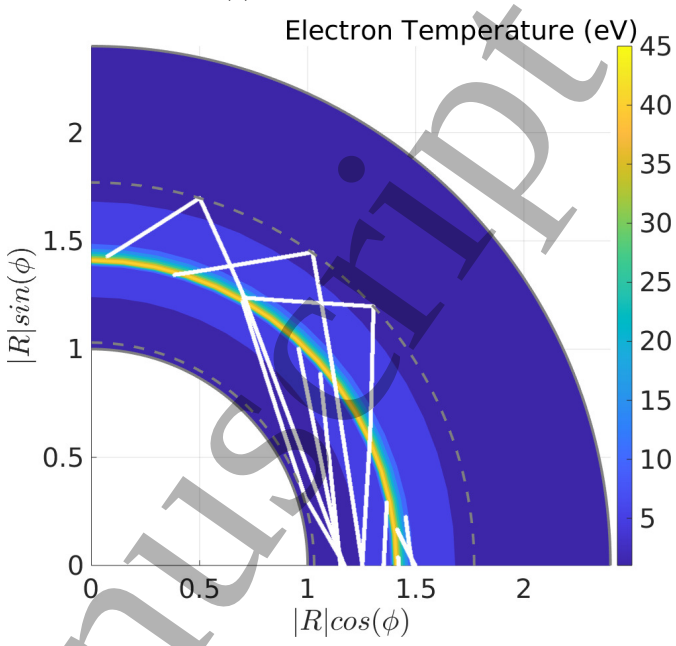

(b) Long trajectories.

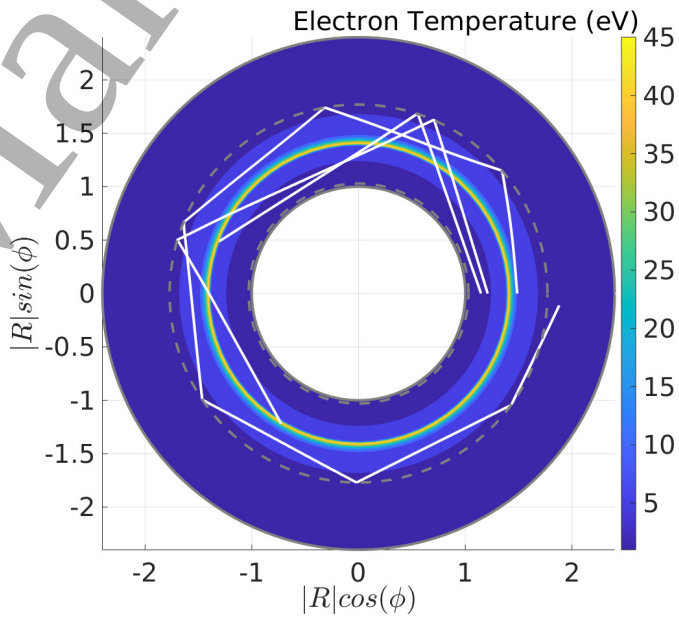

FIG. 11: Plan view of example short (11a) and long (11b) trajectories of simulated particles (white) over the simulated electron temperature at $z = 1.25m$ (coloured) and radial boundaries at $z = 1.25$ (grey dashed).

vertical velocity was zero, the majority of particles remain at this vertical location close to the divertor floor. The dashed grey lines at $R = 1.03m$ and $R = 1.77m$ indicates the inner wall at $z = -1.25m$, with many particles reflected following collisions with this boundary. The trajectories of simulated dust were observed to terminate most frequently at the outer divertor strike point, with some larger dust with greater initial velocity able to sur-

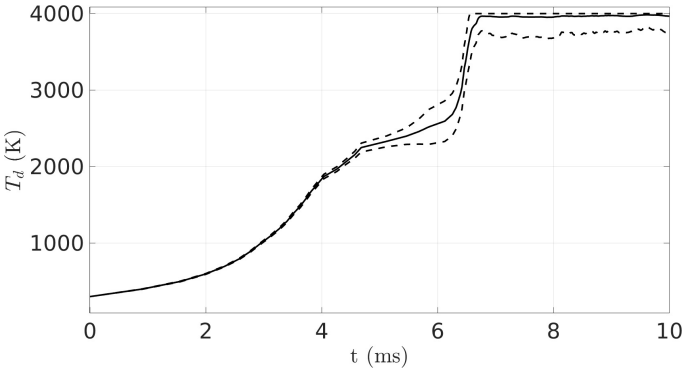

FIG. 12: Average temperature evolution of simulated graphite dust in DIII-D.

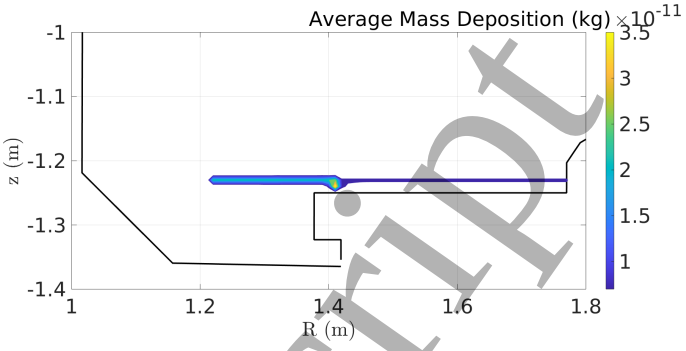

FIG. 13: Average mass ablated by simulated graphite dust at the lower divertor.

vive transitioning this region and reflecting following impacts with the outer wall. This is demonstrated by figure 11a with representative tracks initially at $R \simeq 1.4m$ being far shorter and most dust grain lifetimes being principally determined by the time required to reach the strike point. The largest force experienced by the majority of simulated dust grains was the ion drag force, equation 8. However this force was not great enough to maintain particle velocity in the toroidal direction. Some examples of longer trajectories are shown in figure 11b that rebound multiple times and have comparatively longer lifetimes surviving in the outer divertor.

The average temperature evolution of the 200 graphite dust grains for $t < 10ms$ is shown in figure 12. Almost all dust grains initially experience a similar evolution from $300K$ to $2500K$ before the cooling processes balance the plasma heating. At disparate times, the temperature becomes high enough for thermionic electron emission to dominate, causing dust grains to become positively charged, increasing the plasma heat fluxes and dust temperature to $4000K$ when it begins to sublimate. Some dust grains experience cooler regions of plasma and survive for extended periods close to the outer wall. Eventually all dust grain tracks terminate after falling below the lower mass limit due to ablation.

Without a significant vertical velocity component, the majority of the mass was sublimated in a small region close to the divertor floor. This is shown in figure 13, where the average mass of a simulated carbon particle sublimated across a poloidal cross section is shown. A peak of $3.5 \times 10^{-11} kg$ in the deposition profile occurs at $R \simeq 1.4m$ corresponding to the outer divertor strike point and destruction of the majority of dust grains at this radial location.

Through combining the output of DTOKS with the visualisation software Calcam[61], synthetic diagnostic data for the fast imaging visual cameras was generated. Comparing the tracks in figure 14, qualitative agreement is observed with the synthetic data, demonstrating the utility of this technique for predicting observations and benchmarking dust transport codes. In particular, the simulated paths show similar radial acceleration and track lengths. The small erratic movements of some particles were not well replicated however. Both experimental and simulated trajectories appear to terminate close to the outer strike point. However many of the simulated tracks are far longer than those observed experimentally. The mean simulated lifetime was found to be $11 \pm 2ms$. The discrepancy between this simulated lifetime and the observed lifetime of $\tau_{exp} = 2.1 \pm 0.4ms$ is most likely due to the dust only being detectable by the visible camera for temperatures greater than $\sim 2500K$[64]. Ignoring the extremely long trajectories with initial radial coordinates $R > 1.6m$ which survive mostly outside the camera field of view and subtracting the average simulated time required for dust to reach $2500K$ of $5.9 \pm 0.4ms$ as shown in figure 12, the corrected simulated lifetime is estimated to be $1.5 \pm 0.2ms$.

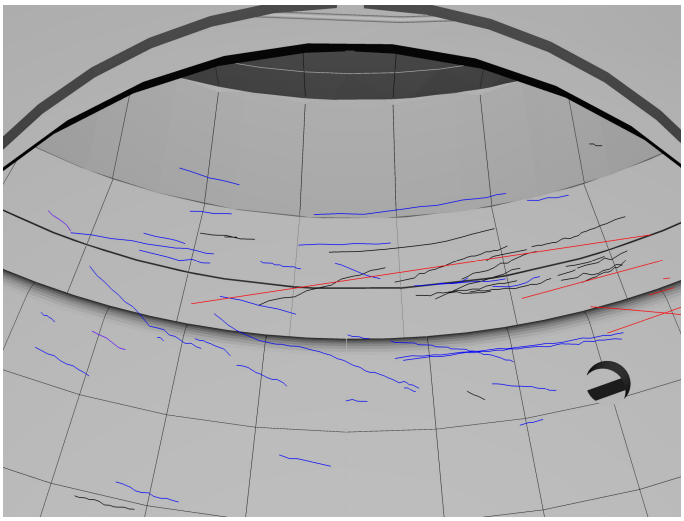

FIG. 14: Reconstructed synthetic visual camera data rendered using Calcam[61] showing dust grain tracks as simulated with DTOKS-U (red) and from S167342 (blue) and S167345 (black) identified using RIDAT as shown previously in figure 8c.

VI. CONCLUSIONS

The advances in the simulation methodology of DTOKS-U have been presented, extending the modelling capabilities to account for a wider range of dust and plasma conditions. More accurate modelling of the temperature and size dependence of the standard values of material properties, in particular the emissivity, heat capacity and thermal expansion coefficient were found to have a significant effect; halving the predicted particle lifetimes of graphite dust in a steady state test case and increasing the equilibrium temperature by $200K$. This underlines the importance of accurately modelling the detailed material properties of dust in these simulations.

Novel observations of carbon dust transport in the DIII-D tokamak performed using the machine learning algorithm RIDAT were compared to integrated DTOKS-U simulations. A total of 932 tracks were identified by RIDAT across two comparable plasma discharges in the DIII-D tokamak. For the 53 unique particles travelling under nominal plasma conditions, a mean observation time was measured, $\tau_{exp} = 2.1 \pm 0.4ms$, with particle velocities found to be predominantly in the direction of the toroidal ion flow. The velocity distributions were fit with a normal ($\mu = -21.0, \sigma = 15.0$) and log-normal ($\mu = 51.0, \sigma = 0.6$) distribution in the radial and toroidal directions respectively. The mean toroidal and radial acceleration of particles was estimated as $a_\theta = 15 \pm 3kms^{-2}$ and $a_R = -4.1 \pm 2.6kms^{-2}$ though many particles were found to not experience a detectable acceleration and a large spread in values was observed. The majority of trajectories were found to terminate close to the outer divertor strike point.

Stochastic modelling of 200 graphite particles was performed by DTOKS-U using initial conditions informed by experimental measurements of velocity and size distributions. The mean simulated lifetime of $\sim 11 \pm 2ms$ only approximated the experimental lifetime after correcting for dust visibility and ignoring the particles with longer trajectories, giving $\sim 1.5 \pm 0.2ms$. Simulated trajectories were found to ablate rapidly after acquiring a positive charge in the intense plasma of the outer strike point at $R \sim 1.4m$ creating an acute source of impurities. This agreement with experimental observation suggests the strike point may play an underappreciated role in limiting dust transport across the divertor floor. However, without a direct quantitative comparison with experiment, it is not possible to validate the relative effect of the various charging models introduced, the changes to thermionic electron emission or the impact of mass loss through evaporation.

The lack of information about initial conditions provided by experimental diagnostics and the single camera view limits comparative analysis with simulation due to the large number of uncontrolled variables and free parameters of simulations. To rigorously test the theoretical models used, pre-characterised particles and additional diagnostics are required to restrict the parameter space of initial conditions. Planned experiments on DIII-D and MAST will aim to use multiple visual cameras and intense plasma conditions to provide a greater insight into the behaviour of molten metal droplets in tokamak plasmas.

VII. ACKNOWLEDGEMENTS

The authors would like to acknowledge the work of Prof. Oliver Schmitz the session leader for these experiments and the work of Guoliang Xu for providing OEDGE plasma simulation data. This work was supported in part by the US Department of Energy under DE-FC02-04ER54698 and DE-FG02-07ER5491.

[1] P. K. Shukla, Phys. Plasmas 8, 1791 (2001).
[2] R. L. Merlino and J. Goree, Phys. Today (2004).
[3] V. E. Fortov, Physica 90 (2004).
[4] S. I. Krasheninnikov, a Y. Pigarov, R. D. Smirnov, M. Rosenberg, Y. Tanaka, D. J. Benson, T. K. Soboleva, T. D. Rognlien, D. a Mendis, B. D. Bray, D. L. Rudakov, J. H. Yu, W. P. West, a L. Roquemore, C. H. Skinner, J. L. Terry, B. Lipschultz, a Bader, R. S. Granetz, C. S. Pitcher, N. Ohno, S. Takamura, S. Masuzaki, N. Ashikawa, M. Shiratani, M. Tokitani, R. Kumazawa, N. Asakura, T. Nakano, a M. Litnovsky, and R. Maqueda, Plasma Phys. Control. Fusion 50, 124054 (2008).
[5] J. Blum, A. C. Levasseur-Regourd, O. Munoz, R. J. Slobodrian, and A. Vedernikov, Europhys. 39, 225 (2008).
[6] H. B. Garrett, Rev. Geophys. 19, 577 (1981).
[7] H. M. Mott-Smith and I. Langmuir, Phys. Rev. 28, 727 (1926).
[8] I. Mann, N. Meyer-Vernet, and A. Czechowski, Phys. Rep. 536, 1 (2014).
[9] R. Neu, R. Dux, A. Geier, O. Gruber, A. Kallenbach, K. Krieger, H. Maier, R. Pugno, V. Rohde, and S. Schweizer, Fusion Eng. Des. 65, 367 (2003).
[10] J. Roth, E. Tsitrone, T. Loarer, V. Philipps, S. Brezinsek, A. Loarte, G. F. Counsell, R. P. Doerner, K. Schmid, O. V Ogorodnikova, and R. A. Causey, Plasma Phys. Control. Fusion 50, 103001 (2008).
[11] R. C. Isler, R. V. Neidigh, and R. D. Cowan, Phys. Lett. A 63, 295 (1977).
[12] L. R. Baylor, N. Commaux, T. C. Jernigan, N. H. Brooks, S. K. Combs, T. E. Evans, M. E. Fenstermacher, R. C. Isler, C. J. Lasnier, S. J. Meitner, R. A. Moyer, T. H. Osborne, P. B. Parks, P. B. Snyder, E. J. Strait, E. A. Unterberg, and A. Loarte, Phys. Rev. Lett. 110, 1 (2013).
[13] D. L. Rudakov, C. P. Chrobak, R. P. Doerner, S. I. Krasheninnikov, R. A. Moyer, K. R. Umstadter, W. R. Wampler, and C. P. C. Wong, J. Nucl. Mater. 438, S805 (2013).
[14] A.G. Guézennec, J.C. Huber, F. Patisson, P. Sessiecq, J.P. Birat, and D. Ablitzer, ISIJ Int. 44, 1328 (2004).
[15] A.T. Peacock, P. Andrew, P. Cetier, J.P. Coad, G. Federici, F.H. Hurd, M.A. Pick, and C.H. Wu, J. Nucl. Mater. 266, 423 (1999).
[16] W.J. Carmack, R.A. Anderl, R.J. Pawelko, G.R. Smolik, and K.A. McCarthy, Fusion Eng. Des. 51–52, 477 (2000).
[17] S.J. Piet, A. Costley, G. Federici, F. Heckendorn, and R. Little, Proc. - Symp. Fusion Eng. 1, 167 (1998).
[18] J. Roth, E. Tsitrone, A. Loarte, T. Loarer, G. Counsell, R. Neu, V. Philipps, S. Brezinsek, M. Lehnen, P. Coad, C. Grisolia, K. Schmid, K. Krieger, A. Kallenbach, B. Lipschultz, R. Doerner, R. Causey, V. Alimov, W. Shu, O. Ogorodnikova, A. Kirschner, G. Federici, and A. Kukushkin, J. Nucl. Mater. 390–391, 1 (2009).
[19] G. R. Longhurst and L. L. Snead, (2004).
[20] J. E. Allen, Phys. Scr. 45, 497 (1992).
[21] J. Winter, Plasma Phys. Control. Fusion 46, B583 (2004).

[22]S. I. Krasheninnikov, R. D. Smirnov, and D. L. Rudakov, Plasma Phys. Control. Fusion 53, 083001 (2011).
[23]A. Autricque, S. H. Hong, N. Fedorczak, S. H. Son, H. Y. Lee, I. Song, W. Choe, and C. Grisolia, Nucl. Matter. Energy 12, 599 (2017).
[24]R. D. Smirnov, A. Y. Pigarov, M. Rosenberg, S. I. Krasheninnikov, and D. a Mendis, Plasma Phys. Control. Fusion 49, 347 (2007).
[25]G. Gervasini, E. Lazzaro, and A. Uccello, J. Fusion Energy 36, 25 (2017).
[26]L. Vignitchouk, P. Tolias, and S. Ratynskaia, Plasma Phys. Control. Fusion 56, 095005 (2014).
[27]J. M. Shull, Astrophys. J. 226, 858 (1978).
[28]C. T. N. Willis, M. Coppins, M. Bacharis, and J.E. Allen, Phys. Rev. E 85, 36403 (2012).
[29]J. H. Yu, D. L. Rudakov, A. Y. Pigarov, R. D. Smirnov, N. H. Brooks, S. H. Muller, and W. P. West, J. Nucl. Mater. 390–391, 216 (2009).
[30]S. K. Combs, S. J. Meitner, T. E. Gebhart, L. R. Baylor, J. B. O. Caughman, D. T. Fehling, C. R. Foust, T. Ha, M. S. Lyttle, J. T. Fisher, and T. R. Younkin, Proc. - Symp. Fusion Eng. 2016–May, (2016).
[31]N. Commaux, D. Shiraki, L. R. Baylor, E. M. Hollmann, N. W. Eidietis, C. J. Lasnier, R. A. Moyer, T. C. Jernigan, S. J. Meitner, S. K. Combs, and C. R. Foust, Nucl. Fusion 56, (2016).
[32]L. Vignitchouk, S. Ratynskaia, and P. Tolias, Plasma Phys. Control. Fusion 59, (2017).
[33]N. Rizopoulou and M. Bacharis, Phys. Plasmas 25, (2018).
[34]J. T. Holgate, L. Simons, Y. Andrew, C. K. Stavrou, and J. E. T. Contributors, Eur. Phys. Lett. 127, 1 (2019).
[35]J.D. Martin, M. Coppins, and G.F. Counsell, J. Nucl. Mater. 337–339, 114 (2005).
[36]G. De Temmerman, M. Bacharis, J. Dowling, and S. Lisgo, Nucl. Fusion 50, 105012 (2010).
[37]J.C. Flanagan, M. Sertoli, M. Bacharis, G.F. Matthews, P.C. de Vries, A. Widdowson, I.H. Coffey, G. Arnoux, B. Sieglin, S. Brezinsek, J.W. Coenen, S. Marsen, T. Craciunescu, A. Murari, D. Harting, A. Cackett, and E. Hodille, Plasma Phys. Control. Fusion 57, 014037 (2015).
[38]J.D. Martin, M. Bacharis, M. Coppins, G.F. Counsell, and J.E. Allen, Epl 83, 65001 (2008).
[39]M. Bacharis, M. Coppins, W. Fundamenski, and J.E. Allen, Plasma Phys. Control. Fusion 54, 085010 (2012).
[40]L. Simons and M. Coppins, Phys. Plasmas 27, 063702 (2020).
[41]D. M. Thomas and J. T. Holgate, Plasma Phys. Control. Fusion 59, 25002 (2016).
[42]C. B. Alcock, V. P. Itkin, and M. K. Horrigan, Can. Metall. Q. 23, 309 (1984).
[43]V. E. Fortov, A. V. Ivlev, S. A. Khrapak, A. G. Khrapak, and G. E. Morfill, Phys. Rep. 421, 1 (2005).
[44]P.S. Epstein, Phys. Rev. 23, 710 (1924).
[45]M. Bacharis, M. Coppins, and J. E. Allen, Phys. Plasmas 17, (2010).
[46]S. A. Khrapak, A. V. Ivlev, S. K. Zhdanov, and G. E. Morfill, Phys. Plasmas 12, 1 (2005).
[47]G. Mie, Ann. Phys. 330, 377 (1908).
[48]M. Rosenberg, R. D. Smirnov, and a Y. Pigarov, J. Phys. D. Appl. Phys. 41, 015202 (2007).
[49]W. J. Wiscombe, Appl. Opt. 19, 1505 (1980).
[50]M. A. Abdou, A. H. Hadid, A. R. Raffray, M. S. Tillack, T. Iizuka, P. J. Gierszewski, R. J. Puigh, D. K. Sze, and B. Picologlou, Fusion Eng. Des. 6, 3 (1988).
[51]P. D. Desai, J. Phys. Chem. Ref. Data 15, 967 (1986).
[52]P. S. Gaal, 102, 102 (2009).
[53]A. Cezairliyan and J. L. McClure, Res. Natl. Bur. Stand 75, 283 (1971).
[54]A. T. D. Butland and R. J. Maddison, J. Nucl. Mater. 49, 45 (1973).
[55]M. Chase, J. Phys. Chem. Ref. Data, Monogr. 9 1952 (1998).
[56]J. Roth, J. Nucl. Mater. 266, 51 (1999).
[57]C. Antoine, Comptes Rendus Des Séances l'Académie Des Sci. 107, 681 (1888).
[58]L.D. Koffman, M.S. Plesset, and L. Lees, Phys. Fluids 27, 876 (1984).
[59]E.W. Thomas, R.K. Janev, and J. Smith, Nucl. Inst. Methods Phys. Res. B 69, 427 (1992).
[60]S. Dushman, Phys. Rev. 21, 623 (1923)
[61]S. Silburn, calcam version 2.2, https://euratom-software.github.io/calcam/html/index.html, Accessed: 18/07/19
[62]C. Cowley, P. Fuller, Y. Andrew, L. James, L. Simons, M. Sertoli, S. Silburn, A. Widdowson, I. Bykov, D. Rudakov, T. Morgan, and J. Contributors, Phys. Rev. E (2020).
[63]G. Xu, J. Guterl, T. Abrams, H. Q. Wang, J. D. Elder, E. Unterberg, D. M. Thomas, P. C. Stangeby, H. Guo, and M. Ye, Nucl. Fusion 0 (2019).
[64]R.D. Smirnov, S.I. Krasheninnikov, J.H. Yu, A.Y. Pigarov, M. Rosenberg, and J.L. Terry, Plasma Phys. Control. Fusion 51, (2009).